

A nebular origin for the persistent radio emission of fast radio bursts

<https://doi.org/10.1038/s41586-024-07782-6>

Received: 22 December 2023

Accepted: 3 July 2024

Published online: 7 August 2024

 Check for updates

Gabriele Bruni¹✉, Luigi Piro¹, Yuan-Pei Yang^{2,3}, Salvatore Quai^{4,5}, Bing Zhang^{6,7}, Eliana Palazzi⁵, Luciano Nicastro⁵, Chiara Feruglio^{8,9}, Roberta Tripodi^{8,9,10}, Brendan O'Connor¹¹, Angela Gardini¹², Sandra Savaglio^{5,13,14}, Andrea Rossi⁵, Ana M. Nicuesa Guelbenzu¹⁵ & Rosita Paladino¹⁶

Fast radio bursts (FRBs) are millisecond-duration, bright (approximately Jy) extragalactic bursts, whose production mechanism is still unclear¹. Recently, two repeating FRBs were found to have a physically associated persistent radio source of non-thermal origin^{2,3}. These two FRBs have unusually large Faraday rotation measure values^{2,3}, probably tracing a dense magneto-ionic medium, consistent with synchrotron radiation originating from a nebula surrounding the FRB source^{4–8}. Recent theoretical arguments predict that, if the observed Faraday rotation measure mostly arises from the persistent radio source region, there should be a simple relation between the persistent radio source luminosity and the rotation measure itself^{7,9}. Here we report the detection of a third, less luminous persistent radio source associated with the repeating FRB source FRB 20201124A at a distance of 413 Mpc, substantially expanding the predicted relation into the low luminosity–low Faraday rotation measure regime ($<1,000 \text{ rad m}^{-2}$). At lower values of the Faraday rotation measure, the expected radio luminosity falls below the limit-of-detection threshold for present-day radio telescopes. These findings support the idea that the persistent radio sources observed so far are generated by a nebula in the FRB environment and that FRBs with low Faraday rotation measure may not show a persistent radio source because of a weaker magneto-ionic medium. This is generally consistent with models invoking a young magnetar as the central engine of the FRB, in which the surrounding ionized nebula—or the interacting shock in a binary system—powers the persistent radio source.

FRB 20201124A is a repeating fast radio burst (FRB) that underwent a reactivation during March 2021 (refs. 10,11), allowing for an accurate localization with an uncertainty of a few milliarcseconds through very-long-baseline interferometry (VLBI) observations¹². Its precise localization (milliarcsecond) and close distance (redshift $z = 0.098$) with respect to other FRBs with an identified host galaxy make it an ideal target to study the physical conditions of its surroundings. Following the discovery of an extended radio emission associated with star formation in the FRB 20201124A environment¹³, we targeted the FRB region with deep, sub-arcsec angular resolution Very Large Array (VLA) observations at 15 and 22 GHz. A sub-arcsec resolution is crucial to disentangling a possible compact source from the previously detected diffuse (3–4 kpc) emission, allowing us to assess the presence of a persistent radio source (PRS) associated with the FRB.

Observations at 15 GHz highlight a compact, unresolved emitting region, with a position consistent with the FRB location (see Fig. 1a).

Its flux density outshines the diffuse component from the host galaxy at the same frequency. This bright, compact PRS falls in the southwest region of the extended emission previously discovered at higher frequencies¹³. At 22 GHz, a compact component is still detected, although at a lower significance level of 4σ , at a position consistent with the FRB location and the peak of the 15-GHz component (see Extended Data Fig. 1). The estimated projected physical size at 15 GHz is $\lesssim 700 \text{ pc}$ and a much smaller size cannot be excluded. As also noted in ref. 14, the flux densities measured up to 22 GHz imply that this compact source could not be detected in previous VLBI observations because it was too faint for the image noise level reached in those works—about $10 \mu\text{Jy beam}^{-1}$ (refs. 13,15), at the limit of capabilities for current VLBI arrays.

To derive the spectral shape of the source, we have reimaged and reanalysed the 6-GHz VLA archival data from ref. 14 that have a similar resolution to our observations. We could disentangle the compact PRS from the diffuse star-formation emission and estimate a flux density

¹IAPS – Institute for Space Astrophysics and Planetology, INAF (Istituto Nazionale di Astrofisica), Rome, Italy. ²South-Western Institute for Astronomy Research, Yunnan University, Kunming, China. ³Purple Mountain Observatory, Chinese Academy of Sciences, Nanjing, China. ⁴Dipartimento di Fisica e Astronomia “Augusto Righi”, Università degli Studi di Bologna (UNIBO), Bologna, Italy. ⁵Osservatorio di Astrofisica e Scienza dello Spazio di Bologna, INAF (Istituto Nazionale di Astrofisica), Bologna, Italy. ⁶Nevada Center for Astrophysics, University of Nevada, Las Vegas, NV, USA. ⁷Department of Physics and Astronomy, University of Nevada, Las Vegas, NV, USA. ⁸Osservatorio Astronomico di Trieste, INAF (Istituto Nazionale di Astrofisica), Trieste, Italy. ⁹IFPU: Institute for Fundamental Physics of the Universe, Trieste, Italy. ¹⁰Dipartimento di Fisica, Università degli Studi di Trieste, Trieste, Italy. ¹¹McWilliams Center for Cosmology & Astrophysics, Department of Physics, Carnegie Mellon University, Pittsburgh, PA, USA. ¹²Instituto de Astrofísica de Andalucía, CSIC (Consejo Superior de Investigaciones Científicas), Granada, Spain. ¹³Dipartimento di Fisica, Università della Calabria, Arcavacata di Rende, Italy. ¹⁴Laboratori Nazionali di Frascati, INFN (Istituto Nazionale di Fisica Nucleare), Frascati, Italy. ¹⁵Thüringer Landessternwarte Tautenburg, Tautenburg, Germany. ¹⁶IRA – Istituto di Radioastronomia, INAF (Istituto Nazionale di Astrofisica), Bologna, Italy. ✉e-mail: gabriele.bruni@inaf.it

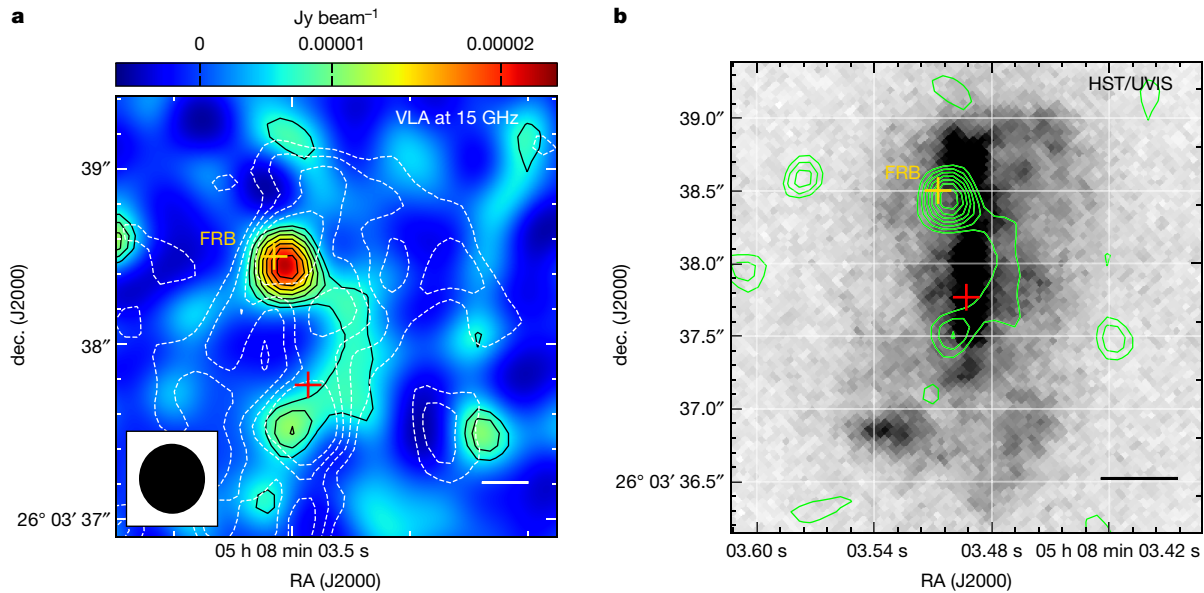


Fig. 1 | Images of the host galaxy of FRB 20201124A. **a**, VLA image at 15 GHz from this work. The angular resolution ($0.38'' \times 0.36''$) is shown as an ellipse in the bottom left corner. Black contours indicate 3σ , 4σ , 5σ , 7σ and 9σ levels. The white contours are from the reimaged 6-GHz VLA archival data¹⁴ at similar resolution and indicate 3σ , 4σ , 5σ and 6σ levels. **b**, HST/UVIS image¹⁴, with

contours reporting the 15-GHz VLA image from **a**. In both panels, the location of the FRB as measured by the European VLBI Network (EVN)¹² is shown by a yellow cross and the centre of the host galaxy as estimated from the HST/UVIS image¹⁴ (F475X optical filter) is shown by a red cross. Scale bars: 500 pc (**a**); 1 kpc (**b**).

consistent with that predicted by those authors on the basis of general image-quality considerations. Considering the flux densities collected from multifrequency (6, 15 and 22 GHz) VLA data, the PRS shows an inverted radio spectrum ($F_\nu \propto \nu^\alpha$, with $\alpha = 1$).

Although the global, diffuse radio emission discussed previously^{13,14,16,17} is linked to star-forming regions in the host galaxy (see Methods), it is difficult to associate the discovered compact radio source with the same physical process. First, the inverted spectrum is unlike the spectral shape observed in radio from star formation, usually steep ($\alpha < -0.5$) or at most flat ($-0.5 < \alpha < -0.2$; see Methods). Furthermore, the radio luminosity of star-forming regions is typically three orders of magnitude lower than the luminosity of the compact radio source. Even the rarest giant regions, with sizes $\lesssim 700$ pc, are ten times less luminous (see Methods). Finally, even assuming a star-formation rate (SFR) capable of accounting for the radio luminosity, it would leave imprints at other wavelengths, which are not detected. Our integral field unit observations with Gran Telescopio Canarias (GTC) MEGARA (see Methods) confirms that the FRB falls at the northern edge of the host galaxy's bar, as seen in previous Hubble Space Telescope (HST) images¹⁴. The SFR map, as estimated from the H α emission line (see Fig. 2), reveals that the highest SFR is towards the centre of the host galaxy and matches the optical emission as seen by HST (see Fig. 1b). Conversely, close to the FRB position, an SFR of around $0.4 M_\odot \text{ yr}^{-1}$ is measured. Furthermore, we performed mm-band observations with the Northern Extended Millimeter Array (NOEMA) centred on the FRB coordinates to independently estimate the SFR through dust grey-body emission. These resulted in two non-detections at 236.5 and 250 GHz, corresponding to 3σ upper limits of $130 \mu\text{Jy beam}^{-1}$ and $160 \mu\text{Jy beam}^{-1}$, respectively. The angular resolution of NOEMA images allowed to investigate a physical scale of about 1.3×0.7 kpc, comparable with that of the VLA. We modelled the cold dust spectral energy distribution (SED) with a modified black body (MBB) function to derive upper limits for the dust mass and SFR (see details in Methods), finding a dust mass of $M_{\text{dust}} < 7.9 \times 10^6 M_\odot$ and a SFR $< 2.2 M_\odot \text{ yr}^{-1}$ at the location of the 15-GHz PRS. However, from our radio images, we could estimate that, to account for the observed radio flux density, a SFR $\gtrsim 3 M_\odot \text{ yr}^{-1}$ would be needed (see Methods). This number is not consistent with either

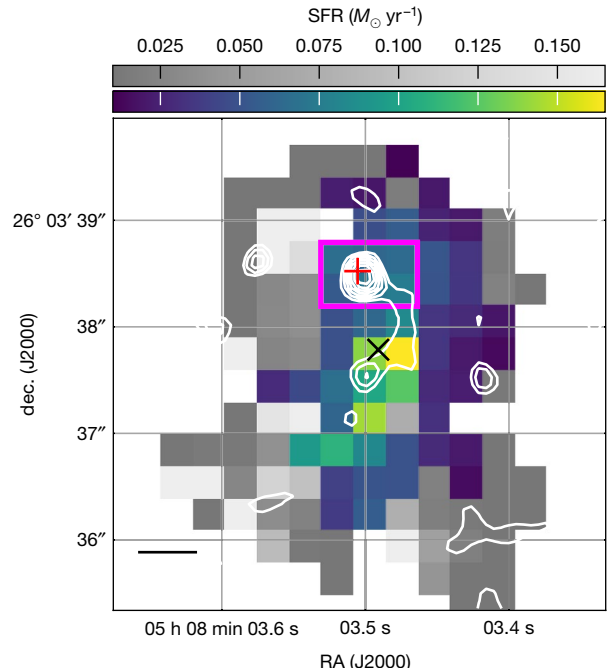


Fig. 2 | SFR map of the FRB 20201124A host galaxy, as derived from GTC/MEGARA integral field spectroscopy. It is estimated from the intrinsic H α luminosity, taking into account galactic and intrinsic dust extinction using the Balmer decrement (H α /H β). Pixels with an H α significance below a 3σ threshold are omitted. In cases in which the H β significance falls below a 2σ threshold—such that no accurate correction for dust extinction is possible—we give a lower limit of the SFR and represent these pixels in greyscale. Note that the tick labels at the top of the two colour bars represent lower-limit SFRs and actual SFRs for greyscale and coloured pixels, respectively. The white contours represent the VLA image at 15 GHz and the red and black crosses represent the FRB and the centre of the host galaxy, respectively. The magenta rectangle defines the galactic region encompassing six adjacent MEGARA pixels surrounding the FRB and PRS zone. Scale bar, 1 kpc.

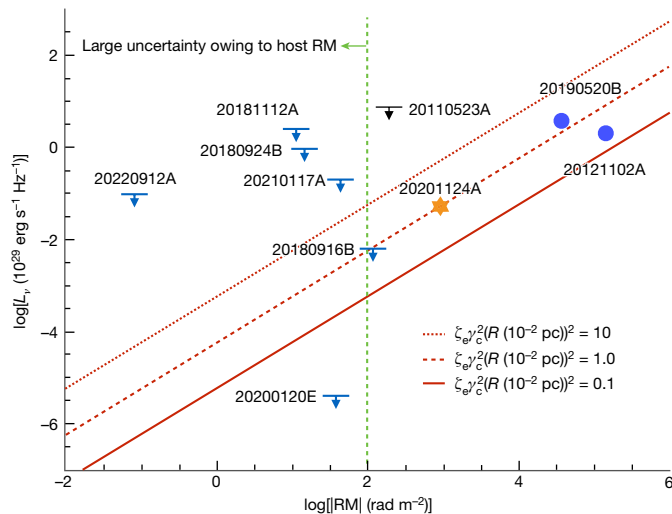


Fig. 3 | The proposed relation between the PRS specific radio luminosity and the FRB RM. The red dotted, dashed and solid lines denote the predicted relations for $\zeta_e \gamma_c^2 (R / 10^{-2} \text{ pc})^2 = 10, 1.0$ and 0.1 , respectively, adopting the nebula model from refs. 7,9. The orange star denotes FRB 20201124A. The black upper limit indicates the non-localized FRB 20110523A with an upper limit of the persistent emission and a measured value of RM, which gives one of the most conservative constraints for non-localized sources in the literature. The blue circles denote the FRBs with measured persistent emission flux and RM (FRB 20121102A and FRB 20190520B). The blue upper limits correspond to the FRBs with precise (arcsecond) localizations. Owing to the large RM uncertainty of the host interstellar medium, the data of FRBs with $|RM| \lesssim (10^2 - 10^3) \text{ rad m}^{-2}$ (on the left side of the green dashed line) might substantially deviate from the predicted relation.

the upper limit from obscured star formation derived from NOEMA observations ($SFR < 2.2 M_\odot \text{ yr}^{-1}$) or the H α -derived SFR at the location of the compact source as estimated from GTC/MEGARA spectroscopy (about $0.4 M_\odot \text{ yr}^{-1}$), further supporting a different origin.

Large Faraday rotation measure (RM) values, $|RM|$, found for some FRBs imply a dense and magnetized environment in the vicinity of the sources^{7,9}. If relativistic electrons constitute a notable fraction of the medium, the magnetized environment near the FRB source could produce synchrotron radiation, powering a bright PRS^{4,9,18,19}. There should be a simple relation between the luminosity of the PRS and the Faraday RM, tracing the magneto-ionic medium in the FRB environment^{7,9}. We consider that the electron distribution in the PRS emission region has a thermal component and a non-thermal component, and the RM is mainly because of the thermal component. As discussed in Methods, the foreseen relation is:

$$L_v \propto (\zeta_e \gamma_c^2 R)^2 \times |RM| \quad (1)$$

in which ζ_e is the fraction of the electrons radiating synchrotron emission in the observed band among all electrons, γ_c is the typical Lorentz factor defined by $\gamma_c^2 = \int n_e(y) dy / \int [n_e(y)/y^2] dy$, $n_e(y)$ is the electron differential distribution with electron Lorentz factor y and R is the radius of the plasma that contributes to the emission of the PRS and the RM.

In Fig. 3, we plot the relation between the specific luminosity (or upper limit) of the PRS against the RM of known FRBs. The red dotted, dashed and solid lines correspond to the predicted relation for $\zeta_e \gamma_c^2 (R / 10^{-2} \text{ pc})^2 = 10, 1.0$ and 0.1 , respectively (see Methods). The observed specific PRS luminosities of FRB 20121102A, FRB 20190520B and FRB 20201124A are close to the predicted value for $\zeta_e \gamma_c^2 (R / 10^{-2} \text{ pc})^2 \approx (0.1 - 10)$. In particular, the detection of the PRS associated with FRB 20201124A allows, for the first time to our knowledge, to test the predicted relation at lower radio luminosity, at the limits of the detection threshold of present-day radio telescopes, thus

substantially broadening the examined parameter space. The upper limit of FRB 20180916B is also close to the predicted relation. As a caveat, we should note that, for FRBs with $RM \lesssim \text{a few } \times 100 \text{ rad m}^{-2}$, the RM from the galactic component or the host component could dominate. This places FRB 20201124A, with $|RM| \approx 900 \text{ rad m}^{-2}$, at the limits of the explorable range.

These findings support a nebular origin for the three detected PRSs associated with FRBs so far. Although the possible nature of the FRB engine itself remains unclear, the nebula model is generally consistent with the proposed scenarios involving a magnetar or a hyperaccreting X-ray binary as the central engine, which already predict an ionized nebula around it^{8,20}. Thanks to the increasing census of FRBs, and in particular repeating ones, deep radio observations of a larger sample of these objects could put further constraints on the nebula model and on the physical conditions in the surroundings of FRBs in general.

Online content

Any methods, additional references, Nature Portfolio reporting summaries, source data, extended data, supplementary information, acknowledgements, peer review information; details of author contributions and competing interests; and statements of data and code availability are available at <https://doi.org/10.1038/s41586-024-07782-6>.

- Zhang, B. The physics of fast radio bursts. *Rev. Mod. Phys.* **95**, 035005 (2023).
- Michilli, D. et al. An extreme magneto-ionic environment associated with the fast radio burst source FRB 121102. *Nature* **553**, 182–185 (2018).
- Niu, C. H. et al. A repeating fast radio burst associated with a persistent radio source. *Nature* **606**, 873–877 (2022).
- Margalit, B. & Metzger, B. D. A concordance picture of FRB 121102 as a flaring magnetar embedded in a magnetized ion-electron wind nebula. *Astrophys. J. Lett.* **868**, L4 (2018).
- Metzger, B. D., Margalit, B. & Sironi, L. Fast radio bursts as synchrotron maser emission from decelerating relativistic blast waves. *Mon. Not. R. Astron. Soc.* **485**, 4091–4106 (2019).
- Yang, G. et al. X-CIGALE: fitting AGN/galaxy SEDs from X-ray to infrared. *Mon. Not. R. Astron. Soc.* **491**, 740–757 (2020).
- Yang, Y.-P., Lu, W., Feng, Y., Zhang, B. & Li, D. Temporal scattering, depolarization, and persistent radio emission from magnetized inhomogeneous environments near repeating fast radio burst sources. *Astrophys. J. Lett.* **928**, L16 (2022).
- Sridhar, N. & Metzger, B. D. Radio nebulae from hyperaccreting X-ray binaries as common-envelope precursors and persistent counterparts of fast radio bursts. *Astrophys. J.* **937**, 5 (2022).
- Yang, Y.-P., Li, Q.-C. & Zhang, B. Are persistent emission luminosity and rotation measure of fast radio bursts related? *Astrophys. J.* **895**, 7 (2020).
- Chime/FRB Collaboration. Recent high activity from a repeating fast radio burst discovered by CHIME/FRB. *The Astronomer's Telegram* **14497**, 1 (2021).
- Lanman, A. E. et al. A sudden period of high activity from repeating fast radio burst 20201124a. *Astrophys. J.* **927**, 59 (2022).
- Nimmo, K. et al. Millisecond localization of the repeating FRB 20201124A. *Astrophys. J. Lett.* **927**, L3 (2022).
- Piro, L. et al. The fast radio burst FRB 20201124A in a star-forming region: constraints to the progenitor and multiwavelength counterparts. *Astron. Astrophys.* **656**, L15 (2021).
- Dong, Y. et al. Mapping obscured star formation in the host galaxy of FRB 20201124A. *Astrophys. J.* **961**, 44 (2024).
- Marcote, B. et al. VLBI localization of FRB 20201124A and absence of persistent emission on millisecond scales. *The Astronomer's Telegram* **14603**, 1 (2021).
- Fong, W.-F. et al. Chronicling the host galaxy properties of the remarkable repeating FRB 20201124A. *Astrophys. J. Lett.* **919**, L23 (2021).
- Ravi, V. et al. The host galaxy and persistent radio counterpart of FRB 20201124A. *Mon. Not. R. Astron. Soc.* **513**, 982–990 (2022).
- Murase, K., Kashiyama, K. & Mészáros, P. A burst in a wind bubble and the impact on baryonic ejecta: high-energy gamma-ray flashes and afterglows from fast radio bursts and pulsar-driven supernova remnants. *Mon. Not. R. Astron. Soc.* **461**, 1498–1511 (2016).
- Metzger, B. D., Berger, E. & Margalit, B. Millisecond magnetar birth connects FRB 121102 to superluminous supernovae and long-duration gamma-ray bursts. *Astrophys. J.* **841**, 14 (2017).
- Margalit, B. et al. Unveiling the engines of fast radio bursts, superluminous supernovae, and gamma-ray bursts. *Mon. Not. R. Astron. Soc.* **481**, 2407–2426 (2018).

Publisher's note Springer Nature remains neutral with regard to jurisdictional claims in published maps and institutional affiliations.

Springer Nature or its licensor (e.g. a society or other partner) holds exclusive rights to this article under a publishing agreement with the author(s) or other rightsholder(s); author self-archiving of the accepted manuscript version of this article is solely governed by the terms of such publishing agreement and applicable law.

© The Author(s), under exclusive licence to Springer Nature Limited 2024

Methods

VLA

Observations with the VLA were performed in B configuration at 15 GHz (Ku band) and 22 GHz (K band), under DDT project 21B-330 (PI: Bruni). The 22-GHz observations were divided into two approximately 2-h blocks and then concatenated to achieve a similar root mean square (r.m.s.) to the 15-GHz ones. Details of observations can be found in Extended Data Table 1. Data calibration was performed with the CASA (<https://casa.nrao.edu/>; ref. 21) VLA pipeline and images deconvolution through the tclean task. The signal-to-noise ratio at 15 GHz allowed us to apply the robust weighting scheme to improve the angular resolution, obtaining a final value for the full width at half maximum (FWHM) similar to the 22-GHz one. The r.m.s. was $2\text{--}3 \mu\text{Jy beam}^{-1}$ at both frequencies.

NOEMA

Observations with the NOEMA were carried out through project W22BS (PI: Bruni) during March 2023 using the B array configuration with 12 antennas. Detail of observations can be found in Extended Data Table 1. The phase centre was set at RA 05 h 08 min 03.470 s, dec. $26^\circ 03' 38.5''$. The band 3 (1 mm) receiver was tuned at 244 GHz, so that the lower side band (LSB) was centred at 236.5 GHz and the upper side band (USB) at 250 GHz. Visibilities were calibrated using the CLID pipeline in the GILDAS software (www.iram.fr/IRAMFR/GILDAS). The absolute flux scale accuracy is on the order of 10%. Imaging and deconvolution were performed using MAPPING applying natural weighting. The final continuum maps reach a 1σ r.m.s. of $4.3 \times 10^{-5} \text{ Jy beam}^{-1}$ in LSB and $5.3 \times 10^{-5} \text{ Jy beam}^{-1}$ in USB. The clean beams are $0.70'' \times 0.42''$ and $0.66'' \times 0.39''$ (PA = 15°) in LSB and USB, respectively.

No clear detection was found in either LSB or USB data towards the FRB position, as derived from 15-GHz VLA data. We derived 3σ upper limits of 0.13 and $0.15 \text{ mJy beam}^{-1}$ in LSB and USB, respectively.

GTC/MEGARA

The GTC/MEGARA instrument^{22,23} collected a series of six observations on 26 October 2022, under project 99-GTC89/22B (PI: Gardini) using the Large Compact Bundle (LCB) Integral Field Unit (IFU) mode. It provides a field of view of $12.5'' \times 11.3''$ using 567 fibres in a hexagonal tessellation with a spaxel size of $0.62''$. To cover the main optical emission lines, useful to derive the SFR spatial distribution in the galaxy, the observations were carried out with two different low-resolution (LR, resolving power $R \approx 6,000$) volume-phase holographic (VPH) gratings, VPH570-LR (LR-V), and VPH675-LR (LR-R), whose specifications can be found in Extended Data Table 1. This produces a combined spectrum covering the spectral range from 4,350 to 7,288 Å (see Extended Data Fig. 4). This range, at the redshift of our target, includes spectral emission lines such as H α , H β , [OIII] and [NII], needed for deriving the spatial distribution of the galaxy parameters such as SFR, intrinsic extinction and velocity map. The measured seeings during the observations were in the range $0.7''\text{--}0.9''$. We used the MEGARA data reduction pipeline v0.12.0 (ref. 24) to process the data. We followed the same procedure as described in detail in ref. 25. The final spectra in which flux was calibrated using the standard star HR 8634 are available in the European Southern Observatory (ESO) spectrophotometric standards database²⁶.

VLA detection of the compact PRS

We detected a compact component at both 15 and 22 GHz. Extended Data Fig. 1 shows the overplot of the image at 6 GHz that we have derived reanalysing archival data from ref. 14 with contours from our 15-GHz and 22-GHz images at similar resolution. The emission comes from regions consistent with the European VLBI Network (EVN) position at all frequencies. Indeed, a Gaussian fit results in a compact component at 15 and 22 GHz, with an integrated flux density of 20.0 ± 3.5 and $30.0 \pm 9.7 \mu\text{Jy}$, respectively. The peak position of the fitted

Gaussian component is RA 05 h 08 min 03.50270 s ± 0.00097 s, dec. $26^\circ 03' 38.444'' \pm 0.014''$ at 15 GHz, whereas it is RA 05 h 08 min 03.4944 s ± 0.0052 s, dec. $26^\circ 03' 38.423'' \pm 0.080''$ at 22 GHz. Considering a standard astrometric accuracy of about 10% of the FWHM and summing that in quadrature with the Gaussian fit error, we get a final uncertainty of $0.04'' \times 0.04''$ at 15 GHz and $0.08'' \times 0.09''$ at 22 GHz. The mentioned positional uncertainties imply that the detected compact component is consistent within 3σ with the FRB location by ref. 12. The measured flux density at 22 GHz accounts for roughly 40% of the value reported at the same frequency, but at lower resolution, in ref. 13, indicating that the previously detected diffuse emission falls below the detection threshold per angular resolution element of the new image.

The image at 6 GHz, and the 15-GHz and 22-GHz images presented here, have a consistent angular resolution and r.m.s. level and can then be used to estimate the spectral index of the compact PRS. At 6 GHz, Dong et al.¹⁴ discuss how a possible PRS would be embedded in a diffuse emission region owing to star formation. Those authors thus provide a conservative upper limit of $10 \mu\text{Jy}$. We reimaged the 6-GHz data from ref. 14 (programme 22A-213; PI: Fong) and performed a further analysis to refine the flux density and compactness estimate of the possible PRS. To account for the diffuse emission, we estimated the mean flux density in the regions contiguous with the FRB location and outside a roughly 1 beam area centred on the component peak at 6 GHz. In this way, we obtained an estimate of $8 \mu\text{Jy beam}^{-1}$ for the emission plateau owing to star formation, consistent with that discussed in ref. 14. We then used this value as an input for the offset parameter of the IMFIT task, which allows to account for a zero-level offset when performing a Gaussian fit on the image. This procedure revealed a compact component at 6 GHz with an integrated flux density of $8.2 \pm 3.8 \mu\text{Jy}$ and centred at RA 05 h 08 min 03.5007 s ± 0.0023 s, dec. $26^\circ 03' 38.5440'' \pm 0.0438''$. As previously discussed, considering an astrometric accuracy of about 10% of the FWHM, we estimate a final uncertainty of $0.05'' \times 0.06''$, again making the peak position consistent with the FRB location within 3σ . We note that, despite the uncertainty on the component flux density being about 45% of the value, it is still at a 4σ detection level with respect to the image r.m.s. ($2 \mu\text{Jy beam}^{-1}$) and 8σ considering its absolute peak of approximately $16 \mu\text{Jy}$ given by the Gaussian + offset fitting. The estimated flux density is also consistent with the upper limit of $10 \mu\text{Jy}$ discussed in ref. 14.

Considering the estimated flux densities at 6, 15 and 22 GHz, we obtain the following spectral indices ($S \propto v^\alpha$) for the PRS: $\alpha_6^{15} = 0.97 \pm 0.54$, $\alpha_{15}^{22} = 1.06 \pm 0.96$ and an overall value $\alpha_6^{22} = 1.00 \pm 0.43$, indicating an inverted spectrum.

SFR estimates from NOEMA observations

To derive upper limits for the dust mass and SFR at the location of the PRS based on the NOEMA fluxes, we modelled the SED of the dust emission with a MBB function given by

$$S_{v_{\text{obs}}}^{\text{obs}} = S_{v/(1+z)}^{\text{obs}} = \frac{\Omega}{(1+z)^3} [B_v(T_{\text{dust}}(z)) - B_v(T_{\text{CMB}}(z))] (1 - e^{-\tau_v}), \quad (2)$$

in which B_v is the black body function that depends on the temperature and rest frequency (v), $\Omega = (1+z)^4 A_{\text{gal}} D_{\text{L}}^{-2}$ is the solid angle with A_{gal} and D_{L} is the surface area and luminosity distance of the galaxy, respectively. The dust optical depth is

$$\tau_v = \frac{M_{\text{dust}}}{A_{\text{galaxy}}} k_0 \left(\frac{v}{250 \text{ GHz}} \right)^\beta, \quad (3)$$

with β the emissivity index and $k_0 = 0.45 \text{ cm}^2 \text{ g}^{-1}$ the mass absorption coefficient²⁷. The solid angle is estimated using the size of the NOEMA beam, which is similar for both observations, $0.7'' \times 0.4''$. The effect of the cosmic microwave background (CMB) on the dust temperature is given by

Article

$$T_{\text{dust}}(z) = ((T_{\text{dust}})^{4+\beta} + T_0^{4+\beta}[(1+z)^{4+\beta} - 1])^{\frac{1}{4+\beta}}, \quad (4)$$

with $T_0 = 2.73$ K. We also considered the contribution of the CMB emission given by $B_\nu(T_{\text{CMB}}(z) = T_0(1+z))$ (ref. 28), even if at this redshift it is almost negligible.

Therefore, this model has three free parameters, T_{dust} , M_{dust} and β . Because we were able to determine only upper limits in the two NOEMA bands, we evaluated possible combinations of T_{dust} and β that can reproduce the limits at 236 GHz and 250 GHz, leaving M_{dust} as a free parameter. Extended Data Fig. 2a presents four models built from reasonable combinations of dust temperature and emissivity, $T_{\text{dust}} = 20, 30$ K and $\beta = 1.5, 2.0$, that are typical values found in local star-forming galaxies^{29,30}. We explored the one-dimensional parameter space using a Markov chain Monte Carlo (MCMC) algorithm implemented in the emcee package³¹ and we assumed a uniform prior for the dust mass, $10^4 M_\odot < M_{\text{dust}} < 10^9 M_\odot$. We obtained $M_{\text{dust}}/10^6 M_\odot = 7.9, 7.8, 4.7, 4.5$ with $[T_{\text{dust}} (\text{K}), \beta] = [20, 1.5], [20, 2.0], [30, 1.5], [30, 2.0]$, from a MCMC with 25 chains, 1,500 trials and a burn-in phase of about 50 for each model.

The SFR is estimated from the total infrared luminosity (TIR) as $\text{SFR} (M_\odot \text{ yr}^{-1}) = 10^{-10} L_{\text{TIR}} (L_\odot)$, assuming Chabrier initial mass function (IMF)³². To compute the TIR luminosity, we integrated the MBB from 8 to 1,000 μm rest frame and therefore we obtained $\text{SFR} = 0.13, 0.34, 0.69$ and $2.24 M_\odot \text{ yr}^{-1}$ for $[T_{\text{dust}} (\text{K}), \beta] = [20, 1.5], [20, 2.0], [30, 1.5]$ and $[30, 2.0]$, respectively. Overall, we obtained $M_{\text{dust}} < 7.9 \times 10^6 M_\odot$ and $\text{SFR} < 2.2 M_\odot \text{ yr}^{-1}$.

To constrain the emission from the host galaxy (see also ref. 14), we recomputed the 3σ upper limits at 236 GHz and 250 GHz considering the region with significance $>3\sigma$ in the 6-GHz VLA map, which corresponds to a physical region of about 2.85 kpc². The 3σ upper limits are then 0.49 mJy and 0.55 mJy at 236 GHz and 250 GHz, respectively. Panel b of Extended Data Fig. 2 shows the best-fitting curves to the new upper limits for $[T_{\text{dust}} (\text{K}), \beta] = [20, 1.5], [20, 2.0], [30, 1.5], [30, 2.0]$. We obtained $1.6 < M_{\text{dust}}/10^7 M_\odot < 2.9$, implying $\text{SFR} < 8.8 M_\odot \text{ yr}^{-1}$.

SFR estimates from GTC/MEGARA observations

Because the emission lines observed in the FRB region and the entire galaxy spectra are produced by ultraviolet radiation from the stellar photosphere (see Supplementary Information), we can thus estimate SFRs directly from the H α intrinsic luminosity. First, we corrected H α for intrinsic dust attenuation based on the Balmer decrement. Extended Data Fig. 3 shows the emission line maps together with the $E(B-V)$ map of the galaxy obtained from the Balmer decrement. The measured line fluxes are reported in Extended Data Table 3. To perform a proper correction for dust extinction, in pixels with $\text{S/N}(H\beta) \geq 2$, the colour excess $E(B-V)$ is derived adopting the attenuation law in ref. 33 and assuming the case B recombination and a Balmer decrement $H\alpha/H\beta = 2.86$ (typical of H II regions with electron temperatures $T_e = 10^4$ K and electron density n_e between 10^2 and 10^4 cm^{-3} (ref. 34)). We assigned $E(B-V) = 0$ to pixels with negative $E(B-V)$ values between about -0.05 and 0 (that is, pixels showing about $2.7 \leq H\alpha/H\beta < 2.86$). Moreover, we also assigned an $E(B-V)$ lower limit to pixels with $\text{S/N}(H\beta) < 2$, using the upper limit in $H\beta$ we defined earlier in this section. The dust-corrected fluxes are converted to luminosity. Then, we derived the SFR using the relation in ref. 35 and the IMF using the relation in ref. 32. We have already shown and discussed the resulting SFR map of the galaxy in Fig. 2. To summarize, we report that, in the stacked spectrum of the FRB region, we measured an SFR of $0.41^{+0.02}_{-0.01} M_\odot \text{ year}^{-1}$, whereas the entire galaxy has an SFR of $4.11^{+0.59}_{-0.53} M_\odot \text{ year}^{-1}$.

Expected radio emission from a star-forming region

Radio emission from star-forming regions typically involves two components: a steep component ($\approx v^{-0.7}$) produced by synchrotron emission from electrons accelerated in supernova explosion, with a lifetime on the order of 100 Myr (ref. 36), which dominates the emission at

low frequencies (below 6 GHz), and a thermal, flat ($\approx v^{-0.5 \leq \alpha \leq -0.2}$) component by Bremsstrahlung, which is a direct measure of the current production of ionized photons by young and hot stars with lifetime < 10 Myr (refs. 37–39). On the other hand, the inverted spectrum observed in the compact radio source is not consistent with either of the star-forming-driven radio components. In Extended Data Fig. 5, we compare the radio spectral slopes for the PRS presented in this work, the nucleus of the host galaxy and the emission of the global host galaxy. The flux densities of the nucleus were collected using the data from ref. 14 (6 GHz) and this work (15 and 22 GHz), whereas for the total radio emission of the host galaxy, we used the lower-resolution VLA observations from our previous work¹³, capable of recovering the emission from extended regions. The slopes clearly indicate a different origin for the emission of the PRS, not consistent with the global steep spectrum of the host galaxy ($\alpha = -0.7$, as also discussed in Supplementary Information) or the nuclear one ($\alpha = -0.5$).

Furthermore, the radio luminosity of star-forming regions in either of the external galaxies is about three orders of magnitude lower than the luminosity of the compact radio source. Even the brightest giant regions, with sizes $\lesssim 700$ pc, are ten times less luminous^{40–43}. Finally, even in the implausible assumption of a star-forming origin, the level of SFR required to account for the observed radio emission would violate the limits derived from mm and H α measurements. The SFR needed to produce the radio thermal component is⁴⁴:

$$\frac{\text{SFR}^T}{M_\odot \text{ yr}^{-1}} = 4.6 \times 10^{-28} \frac{T_e}{10^4 \text{ K}} \nu_{\text{GHz}}^{0.1} \frac{L(\nu_{\text{GHz}})}{\text{erg s}^{-1} \text{ Hz}^{-1}} \quad (5)$$

The observed $L_{15\text{GHz}} = 4.9 \times 10^{27} \text{ erg s}^{-1} \text{ Hz}^{-1}$ would then imply $\text{SFR}^T \gtrsim 3 M_\odot \text{ yr}^{-1}$ to account for the radio emission. This number is not consistent with either the upper limit from obscured star formation derived from the NOEMA or from the H α measurement at the location of the compact source. In principle, the limit from the H α measurement could be alleviated by positing an obscured star formation, but this looks rather unlikely for the following reasons. The fraction of the obscured star formation for this specific galaxy, derived by comparing the SFRs derived from the H α luminosity and the radio luminosity from the whole galaxy, is about 60%, whereas at the FRB position, an obscured fraction of about 90% would be required to account for the radio luminosity. There is no evidence of a stronger obscuration towards the FRB; by contrast, the extinction in that direction is a factor of two lower than towards the centre of the galaxy.

Nebular emission model

We consider that the electron Lorentz factor γ has a differential distribution $n_e(\gamma)$. The total electron number density is then $n_{e,0} = \int n_e(\gamma) d\gamma$. The RM contribution from relativistic electrons is suppressed by a factor of γ^2 owing to the relativistic mass $m_e \rightarrow \gamma m_e$ (ref. 45), thus, the RM contributed by the electrons with the distribution $n_e(\gamma)$ could be approximately written as

$$\text{RM} \simeq \frac{e^3}{2\pi m_e^2 c^4} B_{\parallel} \Delta R \int \frac{n_e(\gamma)}{\gamma^2} d\gamma = \frac{e^3}{2\pi m_e^2 c^4} \frac{n_{e,0} B_{\parallel}}{\gamma_c^2} \Delta R, \quad (6)$$

in which B_{\parallel} is the mean parallel component of the magnetic field along the line of sight, ΔR is the thickness of the nebula and the Lorentz factor γ_c is defined by

$$\gamma_c^2 = \frac{\int n_e(\gamma) d\gamma}{\int [n_e(\gamma)/\gamma^2] d\gamma}. \quad (7)$$

The Lorentz factor of the electrons emitting synchrotron radiation in the observation frequency ν is required to be

$$\gamma_{\text{obs}} \approx \left(\frac{2\pi m_e c v}{eB} \right)^{1/2} \simeq 600 \left(\frac{v}{1 \text{ GHz}} \right)^{1/2} \left(\frac{B}{1 \text{ mG}} \right)^{-1/2}. \quad (8)$$

We define ζ_e as the number fraction of the electrons radiating synchrotron emission in the observed band in all electrons. It can be approximately given by

$$\zeta_e \approx \frac{\gamma_{\text{obs}} n_e (\gamma_{\text{obs}})}{n_{e,0}}. \quad (9)$$

For example, if the electron distribution has a thermal component satisfying the three-dimensional Maxwell distribution in the low-energy regime and a power-law component in the high-energy regime, one would approximately have⁷ $\zeta_e \approx (\gamma_{\text{obs}}/\gamma_c)^{1-p}$, in which p is the distribution index of the high-energy component. Assuming that the magnetic field is large scale (leading to the parallel mean magnetic field on the order of the total magnetic field), then the specific luminosity of synchrotron radiation could be written as^{7,9}

$$L_v = \frac{64\pi^3}{27} \zeta_e \gamma_c^2 m_e c^2 R^2 |\text{RM}| \simeq 5.7 \times 10^{28} \text{ erg s}^{-1} \text{ Hz}^{-1} \\ \times \zeta_e \gamma_c^2 \left(\frac{|\text{RM}|}{10^4 \text{ rad m}^{-2}} \right) \left(\frac{R}{10^{-2} \text{ pc}} \right)^2 \quad (10)$$

in which R is the radius of the plasma screen that contributes to the PRS and the RM.

In Extended Data Table 2, we list 16 FRBs with the measured RM and the measured values (or upper limits) of the flux densities of the PRSs. Only FRB 20121102A, FRB 20190520B and FRB 20201124A have measured values of both. Some sources have precise localizations, so the redshifts in the top row of Extended Data Table 2 are the directly measured values from their host galaxies. For other FRBs, owing to the lack of a precise localization, we estimate their redshifts and luminosity distances by means of the extragalactic dispersion measure (DM), as performed in ref. 9. Note that, for redshift inferred from the excess DM, the corresponding redshift error is attributed to the intergalactic medium density fluctuation^{9,46}.

On the basis of the data in Extended Data Table 2, we plot the relation between the specific luminosity of the PRS and the RM of FRBs in Fig. 3, in which we only list some sources with strong constraints. The red dotted, dashed and solid lines correspond to the predicted relation for $\zeta_e \gamma_c^2 (R/10^{-2} \text{ pc})^2 = 10, 1.0$ and 0.1 , respectively. It is interesting that the observed specific luminosities of FRB 20121102A, FRB 20190520B and FRB 20201124A are close to the predicted value for $\zeta_e \gamma_c^2 (R/10^{-2} \text{ pc})^2 \approx (0.1 - 10)$. The upper limit of FRB 20180916B is close to the predicted relation. However, we should note that, for the FRB, with $\text{RM} \lesssim \text{a few} \times 100 \text{ rad m}^{-2}$, the RM from the galactic component or the host component could dominate.

Considerations on the observed radio spectrum

As pointed out above, the PRS spectrum of FRB 20201124A satisfies $F_v \propto v^l$, which is much harder than those of FRB 20121102A and FRB 20190520B (see Extended Data Fig. 5 for a comparison). If the observed spectrum of the PRS is produced by synchrotron radiation, a spectral index larger than $1/3$ would imply that synchrotron absorption might be dominant at the observed bands (6–22 GHz). Such a high absorption frequency would lead to observed FRBs that are absorbed by the PRS, which is inconsistent with the observation of FRB 20201124A. (For example, for a certain FRB repeater, the absorption process would lead to the spectrum of a radio burst suppressed at a frequency lower than the absorption frequency. This implies that the radio bursts emitted during a limited time would have the same low-frequency cutoff. However, such a feature has not been found so far, even for FRB 20201124A). On the other hand, we note that the spectral index of the PRS is also consistent with $1/3$ within 1.5σ . In this

case, to explain the spectral shape of the PRS, the typical frequency ν_m that corresponds to the minimum Lorentz factor of the accelerated non-thermal electrons is required to be

$$\nu_m \approx \frac{\gamma_m^2 e B}{2\pi m_e c} \gtrsim (22 - 240) \text{ GHz}, \quad (11)$$

in which B is the magnetic field strength at the emission region. Therefore, we obtain the following constraints:

$$\left(\frac{\gamma_m}{10^3} \right)^2 \left(\frac{B}{10 \text{ mG}} \right) \gtrsim (0.8 - 8.6). \quad (12)$$

FRB 20201124A has an RM fluctuation of $\delta\text{RM} \approx 200 \text{ rad m}^{-2}$ on a timescale of 10 days (ref. 47). Its DM fluctuation is not well measured but constrained to be $\delta\text{DM} \lesssim 3 \text{ pc cm}^{-3}$ on a similar timescale. Thus, we can infer $B_{||} > 0.1 \text{ mG}$, which is consistent with the above result. The compact PRS associated with FRB 20201124A might be a magnetized, shocked nebula or an interacting shock in a binary system because of the following reasons. (1) The observed non-thermal emission of the PRS is more likely produced by synchrotron radiation of the accelerated relativistic electrons and shocks are natural locations to accelerate these particles. (2) The typical magnetic field strength $B \approx 10 \text{ mG}$ is much higher than $B \approx 1 \mu\text{G}$ of the interstellar medium⁴⁸. The observations of supernova remnants show that their magnetic field strength is typically approximately a few μG to a few mG (ref. 49). In a binary system, the magnetic field strength in the stellar wind could also be much larger than that in the interstellar medium. (3) There are two main possible scenarios involving a shock region in an astrophysical environment: (1) the interaction between an ejecta and interstellar medium (for example, supernova remnants, afterglows of gamma-ray bursts) or between an electron–positron pair wind and an ejecta (for example, pulsar wind nebulae); (2) an interacting shock between a pair wind and a companion wind in a binary system. The former corresponds to a magnetized shocked nebula and the latter requires that the FRB source is in a binary system. (4) Other radically different combinations of $\gamma_m B$ seem difficult to implement in real astrophysical environments. For example, a much lower $\gamma_m \approx 10$ leads to $B \approx 100 \text{ G}$ according to equation (12). Such a high magnetic field might be in the magnetosphere or the pair wind of a neutron star as the FRB source, but the Lorentz factor of the electrons in these regions should be much higher than $\gamma_m \approx 10$. On the other hand, a much lower magnetic field $B \approx 1 \mu\text{G}$ requires $\gamma_m \approx 10^5$, which means that there are many extremely relativistic electrons in the interstellar medium. However, if these extremely relativistic electrons exist, they should emit and become cool in the near-source environment with a stronger magnetic field.

Finally, if repeating FRBs are indeed powered by a young flaring magnetar embedded in a supernova remnant, an expanding magnetized electron-ion nebula created by the outbursts could naturally contribute to the PRS and the RM of the large burst⁴. Because such a time-dependent model predicts a secular power-law decay of the RM and PRS luminosity, considering that the source number should be proportional to the source age, the RM from a sample of FRB nebulae are predicted to be distributed logarithmically, which could be tested in the future.

Considerations on a possible background source

In the GTC/MEGARA spectrum, we found a detection of a possible emission line in correspondence with the FRB location. If identified as [OII], the emitting source would be at redshift $z = 0.549$. We thus tested the scenario of a background source potentially responsible for the compact radio component, which we instead interpreted as a PRS linked to the FRB.

Deep radio surveys⁵⁰ show that the radio sky at a flux level of about $10 \mu\text{Jy}$ exhibit about 1.4×10^{-3} sources arcsec^{-2} , most of which has a

Article

steep spectrum, unlike the one shown by the source we observe here. Taking into account that only $\lesssim 7\%$ has a flat spectrum, we derive that the probability of one of them falling within the beam size at the position of the FRB is about 10^{-5} . This already results in a very low chance that the radio emission is because of a serendipitous background source. However, in the following, we discuss the different classes of sources that could produce the compact radio component studied in this work and why we can confidently rule them out.

Possible extragalactic sources producing radio emission are blazars, radio galaxies, radio-quiet active galactic nuclei (AGN) or a star-forming galaxy. At the mentioned redshift ($z = 0.549$), the radio luminosity as estimated from our VLA measurement would be $L_R \approx 10^{39} \text{ erg s}^{-1}$, thus indicating a radio-quiet regime. This already rules out a possible background blazar or radio galaxy, although it is still consistent with the faintest (radio-quiet) Seyfert galaxies observed so far in the radio band ($10^{35} < L_R < 10^{39} \text{ erg s}^{-1}$ (ref. 51)). A radio-quiet AGN could show a radio component as a result of a low-power jet, a nuclear wind or coronal emission⁵². In the first case, although the physical scale subtended at $z = 0.549$ by the compact radio component (about 2 kpc) would be enough to accommodate the presence of a jet, the expected radio spectrum of its extended regions would be steep ($\alpha < -0.5$). The inverted radio spectrum we found would thus require a collimated jet with an orientation within a few degrees from the line of sight. This would in turn result in a dominant, Doppler-boosted jet emission visible up to the optical band. This feature has been commonly observed for powerful jets at different scales, from radio-loud AGN to X-ray binaries, but not yet in radio-quiet AGN in which the flat/inverted radio spectrum is attributed to a coronal emission mechanism (refs. 53,54; see also discussion below). Moreover, the NOEMA non-detection in the mm band put a strong constraint on that: a simple power-law extrapolation of the radio spectrum up to 250 GHz results in an expected flux density $> 300 \mu\text{Jy}$, well above the NOEMA upper limit ($< 160 \mu\text{Jy}$). In the second case (nuclear wind), a steep radio spectrum is expected, thus not consistent with the inverted one seen in our VLA measurements. In the third case (AGN coronal emission), a ratio between radio and X-ray luminosity $L_R/L_X \approx 10^{-5}$ is expected⁵⁵, whereas previous Chandra X-ray measurements in a circular region with a 1'' radius centred on the FRB location¹³ constrain this ratio to about 10^{-3} . The X-ray luminosity is thus much lower than that expected from a corona able to produce the radio emission measured with the VLA. Finally, a possible radio emission from a background star-forming galaxy is excluded by the expected relation between [OII] and radio emission in SFR³⁵, foreseeing a radio luminosity about ten times lower than that measured here.

Data availability

All relevant data used for this work are publicly available at the repositories of each facility. In particular, raw and calibrated VLA data can be downloaded from the NRAO data archive (<https://data.nrao.edu/>), NOEMA raw data are available at the IRAM Science Data Archive (<https://iram-institute.org/science-portal/data-archive/>) and GTC raw data at the Gran Telescopio Canarias Public Archive (<https://gtc.sdc.cab.inta-csic.es/gtc/>).

21. CASA Team et al. CASA, the Common Astronomy Software Applications for radio astronomy. *Publ. Astron. Soc. Pac.* **134**, 114501 (2022).
22. Carrasco, E. et al. MEGARA, the R=6000-20000 IFU and MOS of GTC. *Proc. SPIE* **10702**, 1070216 (2018).
23. de Paz, A. G. et al. First scientific observations with MEGARA at GTC. *Proc. SPIE* **10702**, 1070217 (2018).
24. Pascual, S., Cardiel, N., Picazo-Sánchez, P., Castillo-Morales, A. & de Paz, A. G. guaix-ucm/megaradrp: v0.12.0. Zenodo <https://doi.org/10.5281/zenodo.6043992> (2022).
25. Chamorro-Cazorla, M. et al. MEGADES: MEGARA galaxy disc evolution survey. *Astron. Astrophys.* **670**, A117 (2023).
26. Oke, J. B. Faint spectrophotometric standard stars. *Astron. J.* **99**, 1621–1631 (1990).
27. Beelen, A. et al. 350 μm dust emission from high-redshift quasars. *Astrophys. J.* **642**, 694–701 (2006).
28. da Cunha, E. et al. On the effect of the cosmic microwave background in high-redshift (sub-)millimeter observations. *Astrophys. J.* **766**, 13 (2013).
29. Schreiber, C. et al. Dust temperature and mid-to-total infrared color distributions for star-forming galaxies at $0 < z < 4$. *Astron. Astrophys.* **609**, A30 (2018).
30. Lamperti, I. et al. JINGLE – V. Dust properties of nearby galaxies derived from hierarchical Bayesian SED fitting. *Mon. Not. R. Astron. Soc.* **489**, 4389–4417 (2019).
31. Foreman-Mackey, D., Hogg, D. W., Lang, D. & Goodman, J. emcee: the MCMC hammer. *Publ. Astron. Soc. Pac.* **125**, 306 (2013).
32. Chabrier, G. Galactic stellar and substellar initial mass function. *Publ. Astron. Soc. Pac.* **115**, 763–795 (2003).
33. Calzetti, D. et al. The dust content and opacity of actively star-forming galaxies. *Astrophys. J.* **533**, 682–695 (2000).
34. Osterbrock, D. E. & Ferland, G. J. *Astrophysics of Gaseous Nebulae and Active Galactic Nuclei* 2nd edn (University Science Books, 2005).
35. Kennicutt, J. & Robert, C. Star formation in galaxies along the Hubble sequence. *Annu. Rev. Astron. Astrophys.* **36**, 189–232 (1998).
36. Condon, J. J. Radio emission from normal galaxies. *Annu. Rev. Astron. Astrophys.* **30**, 575–611 (1992).
37. Klein, U. & Emerson, D. T. A survey of the distributions of 2.8 cm radio continuum in nearby galaxies. *Astron. Astrophys.* **94**, 29–44 (1981).
38. Gioia, I. M., Gregorini, L. & Klein, U. High frequency radio continuum observations of bright spiral galaxies. *Astron. Astrophys.* **116**, 164–174 (1982).
39. Tabatabaei, F. S. et al. The radio spectral energy distribution and star-formation rate calibration in galaxies. *Astrophys. J.* **836**, 185 (2017).
40. Kennicutt, J. & Robert, C. Structural properties of giant H II regions in nearby galaxies. *Astrophys. J.* **287**, 116–130 (1984).
41. Conti, P. S. & Crowther, P. A. MSX mid-infrared imaging of massive star birth environments – II. Giant H II regions. *Mon. Not. R. Astron. Soc.* **355**, 899–917 (2004).
42. Anderson, L. D. et al. The WISE catalog of galactic H II regions. *Astrophys. J. Suppl. Ser.* **212**, 1 (2014).
43. Anderson, L. D., Bania, T. M., Balser, D. S. & Rood, R. T. The Green Bank Telescope H II region discovery survey. II. The source catalog. *Astrophys. J. Suppl. Ser.* **194**, 32 (2011).
44. Murphy, E. J. et al. Calibrating extinction-free star formation rate diagnostics with 33 GHz free-free emission in NGC 6946. *Astrophys. J.* **737**, 67 (2011).
45. Quataert, E. & Gruzinov, A. Constraining the accretion rate onto Sagittarius A* using linear polarization. *Astrophys. J.* **545**, 842–846 (2000).
46. McQuinn, M. Locating the “missing” baryons with extragalactic dispersion measure estimates. *Astrophys. J. Lett.* **780**, L33 (2014).
47. Xu, H. et al. A fast radio burst source at a complex magnetized site in a barred galaxy. *Nature* **609**, 685–688 (2022).
48. Draine, B. T. *Physics of the Interstellar and Intergalactic Medium* (Princeton Univ. Press, 2011).
49. Reynolds, S. P., Gaensler, B. M. & Bocchino, F. Magnetic fields in supernova remnants and pulsar-wind nebulae. *Space Sci. Rev.* **166**, 231–261 (2012).
50. Richards, E. A. The nature of radio emission from distant galaxies: the 1.4 GHz observations. *Astrophys. J.* **533**, 611–630 (2000).
51. Chiaraluce, E. et al. From radio-quiet to radio-silent: low-luminosity Seyfert radio cores. *Mon. Not. R. Astron. Soc.* **485**, 3185–3202 (2019).
52. Panessa, F. et al. The origin of radio emission from radio-quiet active galactic nuclei. *Nat. Astron.* **3**, 387–396 (2019).
53. Behar, E., Vogel, S., Baldi, R. D., Smith, K. L. & Mushotzky, R. F. The mm-wave compact component of an AGN. *Mon. Not. R. Astron. Soc.* **478**, 399–406 (2018).
54. Chen, S., Laor, A., Behar, E., Baldi, R. D. & Gelfand, J. D. The radio emission in radio-quiet quasars: the VLBA perspective. *Mon. Not. R. Astron. Soc.* **525**, 164–182 (2023).
55. Laor, A. & Behar, E. On the origin of radio emission in radio-quiet quasars. *Mon. Not. R. Astron. Soc.* **390**, 847–862 (2008).
56. The Astropy Collaboration et al. Astropy: a community Python package for astronomy. *Astron. Astrophys.* **558**, A33 (2013).
57. Petroff, E. et al. FRBCAT: the fast radio burst catalogue. *Publ. Astron. Soc. Aust.* **33**, e045 (2016).
58. Planck Collaboration et al. Planck 2018 results. VI. Cosmological parameters. *Astron. Astrophys.* **641**, A6 (2020).
59. Spitler, L. G. et al. Fast radio burst discovered in the Arecibo pulsar ALFA survey. *Astrophys. J.* **790**, 101 (2014).
60. Tendulkar, S. P. et al. The host galaxy and redshift of the repeating fast radio burst FRB 121102. *Astrophys. J. Lett.* **834**, L7 (2017).
61. Marcote, B. et al. The repeating fast radio burst FRB 121102 as seen on milliarcsecond angular scales. *Astrophys. J. Lett.* **834**, L8 (2017).
62. The CHIME/FRB Collaboration et al. CHIME/FRB discovery of eight new repeating fast radio burst sources. *Astrophys. J. Lett.* **885**, L24 (2019).
63. Marcote, B. et al. A repeating fast radio burst source localized to a nearby spiral galaxy. *Nature* **557**, 190–194 (2020).
64. Bannister, K. W. et al. A single fast radio burst localized to a massive galaxy at cosmological distance. *Science* **365**, 565–570 (2019).
65. Prochaska, J. X. et al. The low density and magnetization of a massive galaxy halo exposed by a fast radio burst. *Science* **365**, aay0073 (2019).
66. Anna-Thomas, R. et al. Magnetic field reversal in the turbulent environment around a repeating fast radio burst. *Science* **380**, 599–603 (2023).
67. Bhardwaj, M. et al. A nearby repeating fast radio burst in the direction of M81. *Astrophys. J. Lett.* **910**, L18 (2021).
68. Kirsten, F. et al. A repeating fast radio burst source in a globular cluster. *Nature* **602**, 585–589 (2022).
69. Bhandari, S. et al. A nonrepeating fast radio burst in a dwarf host galaxy. *Astrophys. J.* **948**, 67 (2023).
70. Zhang, Y.-K. et al. FAST observations of FRB 20220912A: burst properties and polarization characteristics. *Astrophys. J.* **955**, 142 (2023).
71. Hewitt, D. M. Milliarcsecond localization of the hyperactive repeating FRB 20220912A. *Mon. Not. R. Astron. Soc.* **529**, 1814–1826 (2024).

72. Masui, K. et al. Dense magnetized plasma associated with a fast radio burst. *Nature* **528**, 523–525 (2015).
73. Petroff, E. et al. A polarized fast radio burst at low Galactic latitude. *Mon. Not. R. Astron. Soc.* **469**, 4465–4482 (2017).
74. Keane, E. F. et al. The host galaxy of a fast radio burst. *Nature* **530**, 453–456 (2016).
75. Ravi, V. et al. The magnetic field and turbulence of the cosmic web measured using a brilliant fast radio burst. *Science* **354**, 1249–1252 (2016).
76. Bhandari, S. et al. The SURvey for Pulsars and Extragalactic Radio Bursts – II. New FRB discoveries and their follow-up. *Mon. Not. R. Astron. Soc.* **475**, 1427–1446 (2018).
77. Caleb, M. et al. The SURvey for Pulsars and Extragalactic Radio Bursts - III. Polarization properties of FRBs 160102 and 151230. *Mon. Not. R. Astron. Soc.* **478**, 2046–2055 (2018).
78. Ostowski, S. et al. Commensal discovery of four fast radio bursts during Parkes Pulsar Timing Array observations. *Mon. Not. R. Astron. Soc.* **488**, 868–875 (2019).
79. Connor, L. et al. A bright, high rotation-measure FRB that skewers the M33 halo. *Mon. Not. R. Astron. Soc.* **499**, 4716–4724 (2020).

Acknowledgements The research leading to these results has received funding from the European Union's Horizon 2020 programme under the AHEAD2020 project (grant agreement no. 871158). B.O. gratefully acknowledges support from the McWilliams Postdoctoral Fellowship at Carnegie Mellon University. Y.-P.Y. is supported by the National Natural Science Foundation of China grant no. 12003028 and the National SKA Program of China (2022SKA0130100). A.G. acknowledges financial support from the Severo Ochoa grant CEX2021-001131-S funded by MCIN/AEI/10.13039/501100011033 and from national project PGC2018-095049-B-C21 (MCIU/AEI/FEDER, UE). The National Radio Astronomy Observatory is a facility of the National Science Foundation operated under cooperative agreement by Associated Universities, Inc. This work is partly based on observations carried out under project number W22BS with the Institut de Radioastronomie Millimétrique (IRAM) Northern Extended Millimeter Array (NOEMA) interferometer. IRAM is supported by INSU/CNRS (France), MPG (Germany) and IGN (Spain).

Partly based on observations made with the Gran Telescopio Canarias (GTC), installed at the Spanish Observatorio del Roque de los Muchachos of the Instituto de Astrofísica de Canarias, on the island of La Palma. This work is partly based on data obtained with MEGARA/MIRADAS instrument, financed by the European Regional Development Fund (ERDF), through Programa Operativo Canarias FEDER 2014–2020. We thank A. G. de Paz (Facultad Ciencias Físicas, Universidad Complutense de Madrid) for his valuable support in the MEGARA data analysis. This research made use of APLpy, an open-source plotting package for Python hosted at <http://aplpy.github.io>. This research made use of Astropy, a community-developed core Python package for astronomy⁵⁶.

Author contributions G.B. led the VLA and NOEMA observational campaigns, conducted the VLA data calibration, analysis and interpretation, and led the paper writing. L.P., Y.-P.Y., B.Z. and S.S. worked on the interpretation of the results. E.P., L.N., S.Q., A.M.N.G. and A.R. conducted the GTC/MEGARA observations, data analysis and interpretation. C.F. and R.T. worked on the NOEMA data calibration and analysis. B.O. realized the host galaxy broad-band SED fitting. A.G. led the GTC/MEGARA proposal. R.P. contributed to the NOEMA proposal preparation. All authors contributed to the discussion of the results presented and commented on the manuscript.

Competing interests The authors declare no competing interests.

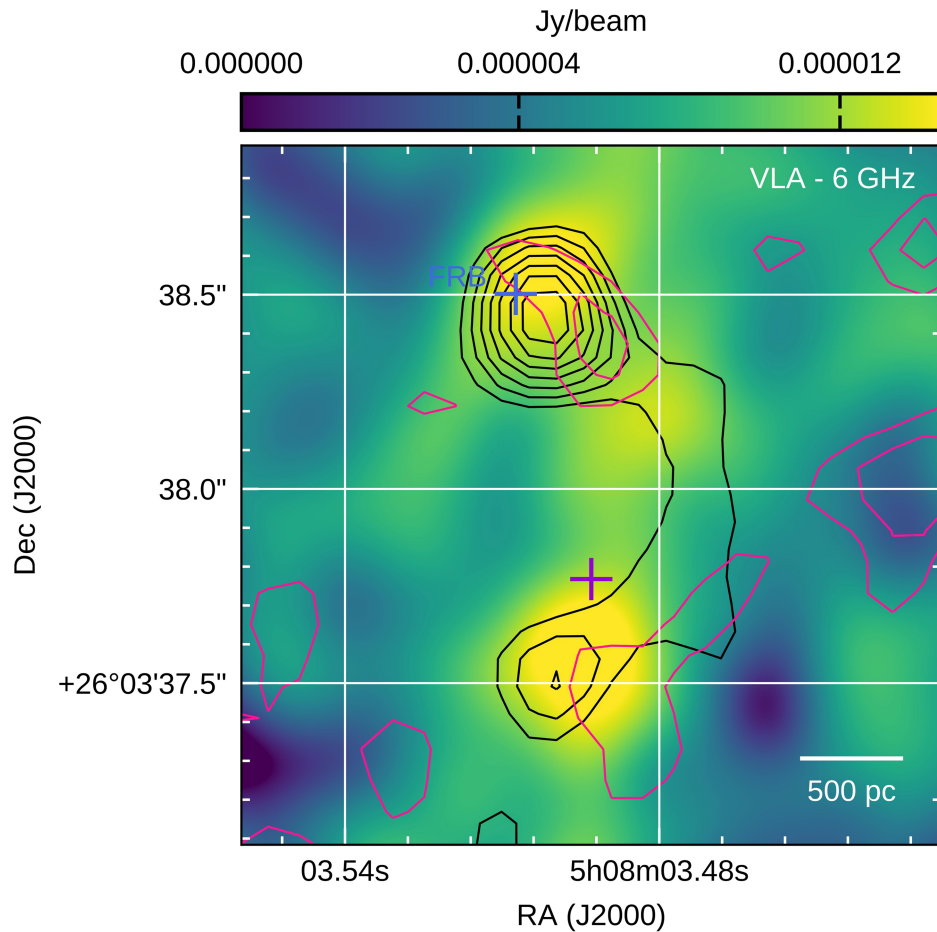
Additional information

Supplementary information The online version contains supplementary material available at <https://doi.org/10.1038/s41586-024-07782-6>.

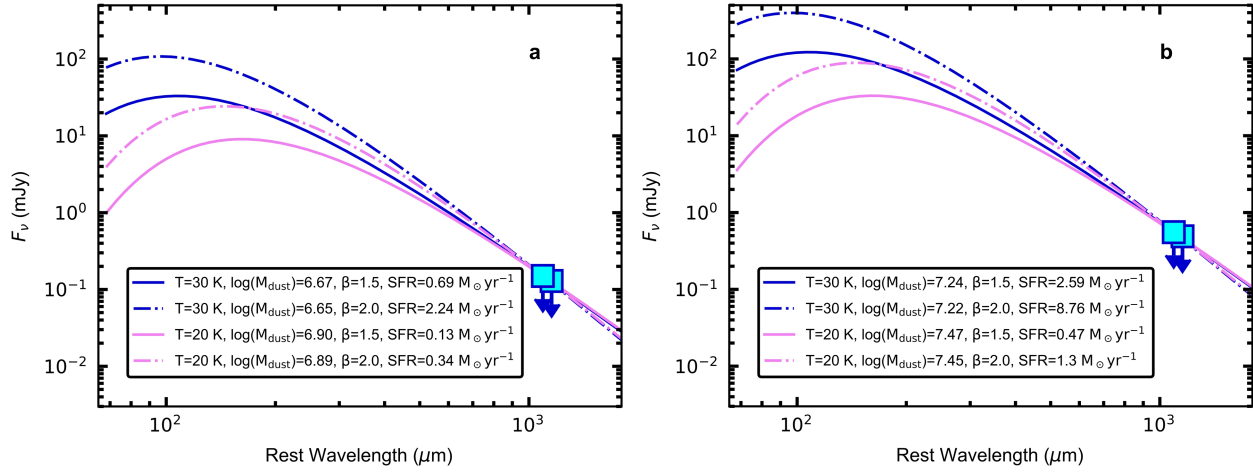
Correspondence and requests for materials should be addressed to Gabriele Bruni.

Peer review information *Nature* thanks the anonymous reviewers for their contribution to the peer review of this work. Peer reviewer reports are available.

Reprints and permissions information is available at <http://www.nature.com/reprints>.



Extended Data Fig. 1 | Multifrequency radio image of the host galaxy of FRB 20201124A. Overplot of the 6-GHz VLA image from ref. 14 (in colour) with contours from the 15-GHz (black) and 22-GHz (red) VLA images from this work. The purple cross indicates the host galaxy centre and the blue cross is the FRB position.

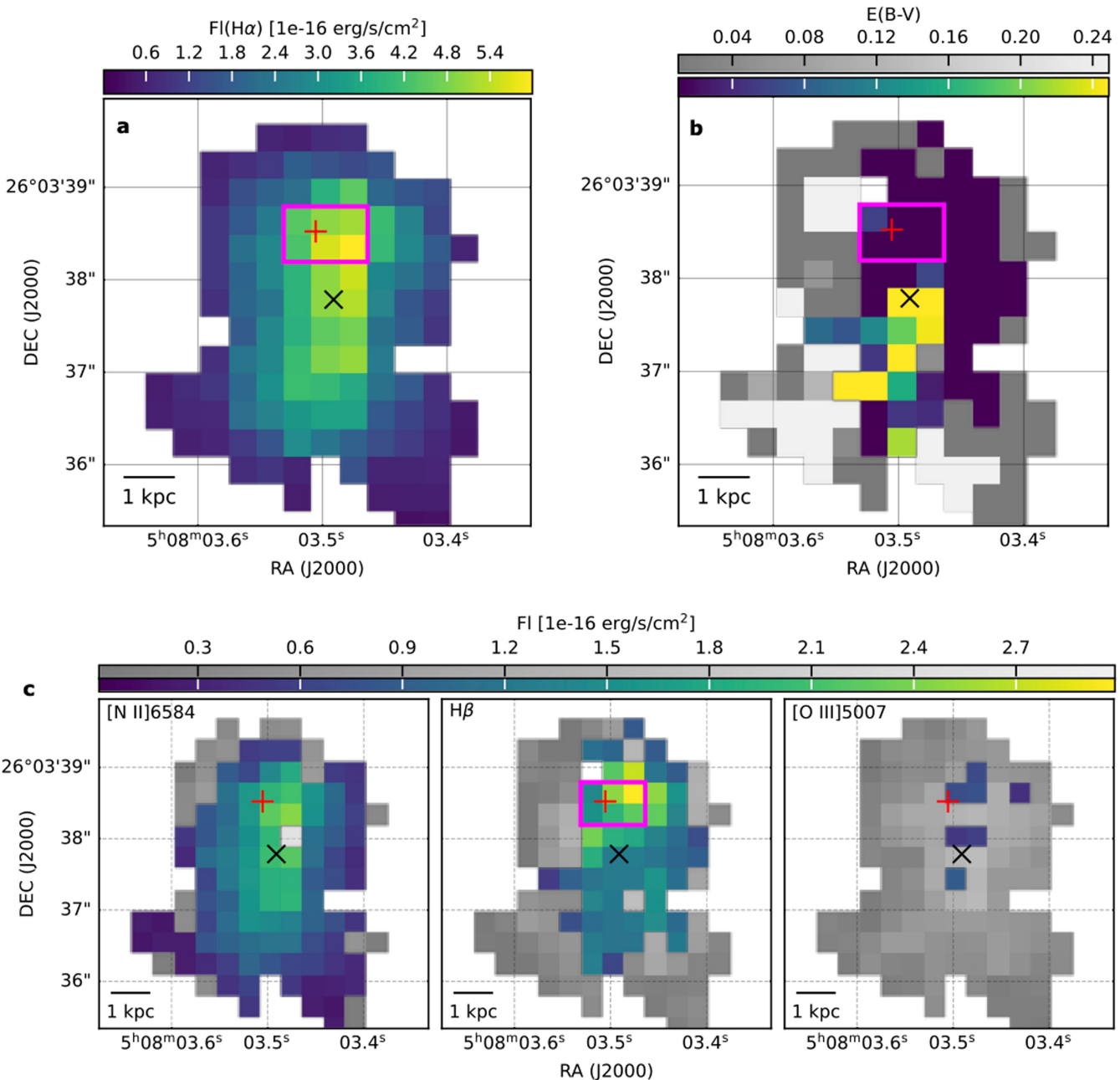


Extended Data Fig. 2 | SEDs of the cold dust emission of FRB 20201124A.

Estimated values are based on the NOEMA upper limits at 236 GHz and 250 GHz (cyan squares). **a**, SED computed in one beam towards the FRB position as seen in the VLA 15-GHz map. The best-fitting curves with fixed $[T_{\text{dust}} (\text{K}), \beta] = [20, 1.5], [20, 2.0], [30, 1.5], [30, 2.0]$ are plotted as solid violet, dashed violet, solid

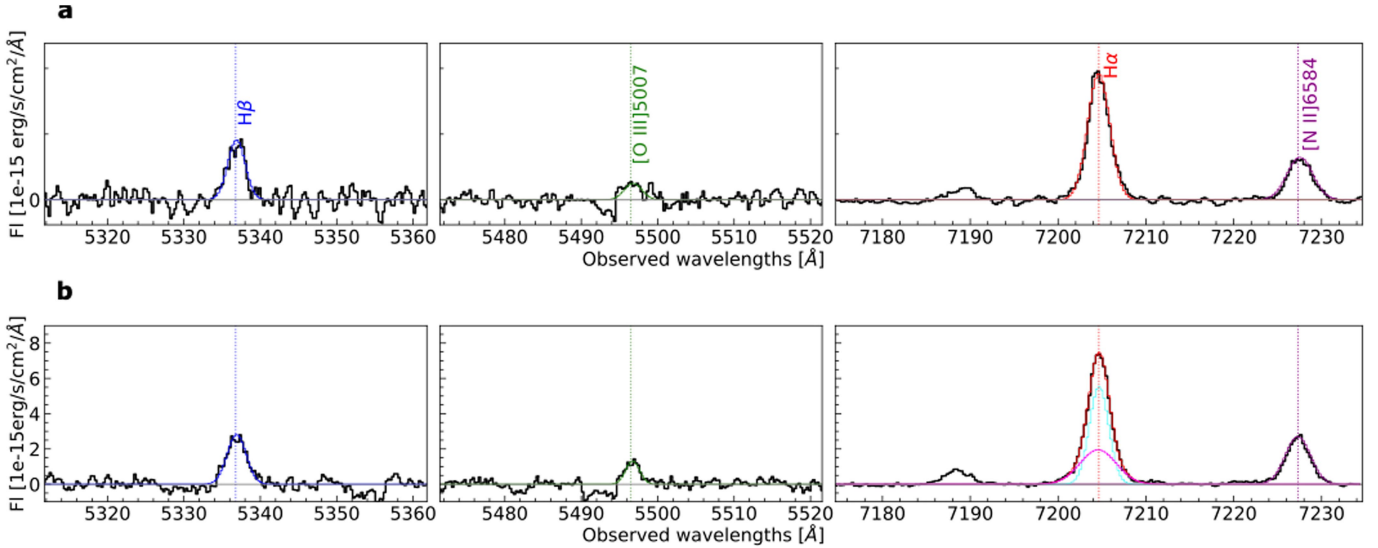
blue and dashed blue lines, respectively. **b**, SED of the cold dust emission of FRB 20201124A based on the NOEMA upper limits at 236 GHz and 250 GHz (cyan squares) computed for the region $>3\sigma$ in the 6-GHz map. The best-fitting curves with fixed $[T_{\text{dust}} (\text{K}), \beta] = [20, 1.5], [20, 2.0], [30, 1.5], [30, 2.0]$ are plotted as solid violet, dashed violet, solid blue and dashed blue lines, respectively.

Article



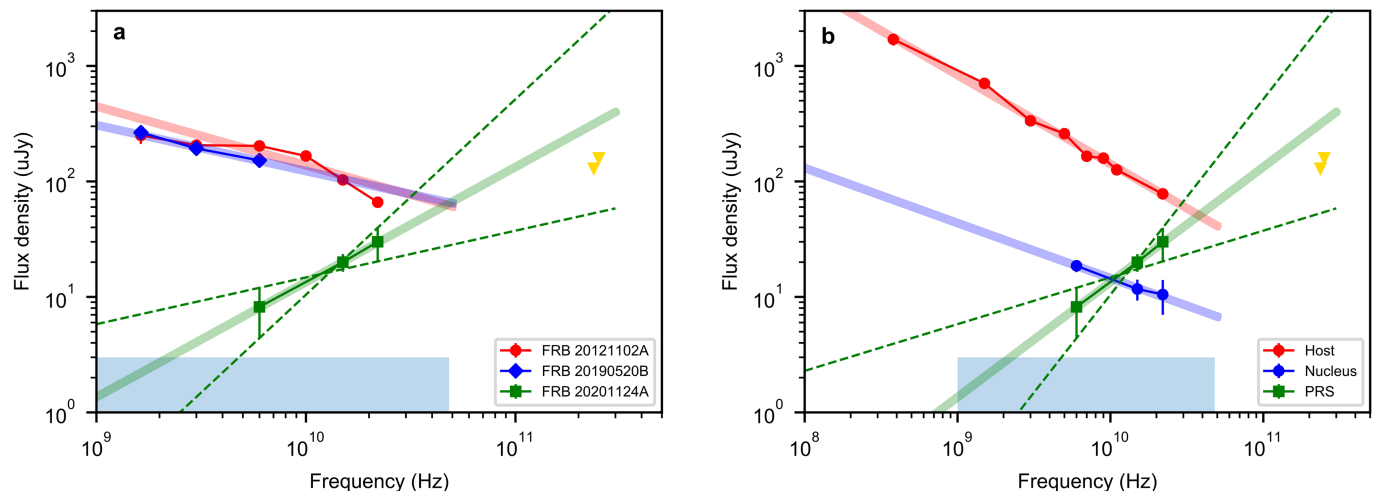
Extended Data Fig. 3 | GTC/MEGARA maps. **a**, Galactic extinction corrected $\text{H}\alpha$ emission line map. **b**, Map of the intrinsic $E(B - V)$ of the galaxy. We estimated the intrinsic $E(B - V)$ taking into account galactic dust extinction and using the Balmer decrement ($\text{H}\alpha/\text{H}\beta$). In cases in which the $\text{H}\beta$ significance falls below a 2σ threshold, no accurate correction for dust extinction is possible. For these pixels, we give a lower limit for the intrinsic $E(B - V)$, shown in greyscale. Note that the tick labels above the two colour bars represent lower limits and actual $E(B - V)$ values for greyscale and coloured pixels, respectively. **c**, Maps of the

emission lines $[\text{N II}] 6584$, $\text{H}\beta$ and $[\text{O III}] 5007$. In cases in which the line significance falls below 2σ we give an upper limit and represent these pixels in greyscale. The tick labels above the two colour bars represent upper flux limits and actual flux values for greyscale and coloured pixels, respectively. The red and black crosses represent the FRB and galactic centre, respectively. The magenta rectangle defines the galactic region encompassing six adjacent MEGARA pixels surrounding the FRB and PRS zone. For all of the maps, pixels with an $\text{H}\alpha$ significance below a 3σ threshold are omitted.



Extended Data Fig. 4 | Stacked GTC/MEGARA spectra. From left to right, $H\beta$, $[O\text{III}] 5007$ and $H\alpha$ regions are presented. **a**, Stacked spectra from the six pixels in the FRB region (as shown in Extended Data Fig. 3). **b**, Stacked spectra of the entire galaxy. Individual spectra were shifted to align with the reference redshift ($z = 0.0978$) before stacking to compensate for any $H\alpha$ -related velocity

effect. Coloured vertical dotted lines mark the centroids of the three lines at the reference redshift. We observe an absorption line at approximately 5,493 Å. However, the nature of this spectral feature remains unrecognized by our analysis. This line is observed in each individual spectrum, too.



Extended Data Fig. 5 | The PRS spectrum. **a**, Radio spectra of the three PRSs known so far. **b**, Radio spectra of the PRS, the nuclear region of the host galaxy and the total emission of the host galaxy. In both panels, power-law fits are reported as solid lines, the green dashed lines indicate the maximum and minimum slope consistent with measurements within errors for the PRS

presented in this work, the yellow triangles represent the NOEMA upper limits for FRB 20201124A and the blue shaded area represents the region not detectable by the VLA, in the range 1–50 GHz (we assume a representative r.m.s. = $1 \mu\text{Jy beam}^{-1}$, reachable in about 10 h at 6 GHz).

Extended Data Table 1 | Details of radio and GTC/MEGARA observations

Telescope	Date	Frequency	Bandwidth	FWHM	P.A.	RMS	Flux density
	dd/mm/yyyy	(GHz)	(GHz)	(arcsec)	(deg)	(μ Jy/beam)	(μ Jy)
VLA [†]	06/03/2022	6	4	0.38×0.36	-51	2.0	8.2 ± 3.8
VLA	07/10/2021	15	6	0.38×0.36	+3.6	2.3	20.0 ± 3.5
VLA	03-07/01/2022	22	8	0.37×0.32	-53	3.0	30.0 ± 9.7
NOEMA	12/03/2023	236.5	7.6	0.7×0.42	+15	43	$< 130^{\ddagger}$
NOEMA	12/03/2023	250	7.6	0.66×0.39	+15	53	$< 160^{\ddagger}$

GTC/MEGARA ⁺	Date	Band	Exposure	R.L.D.*	R [†]
		(\AA)	(s)	($\text{\AA} \text{ px}^{-1}$)	
VPH LR-V	28/10/2022	5165.6 – 6176.2	3×1800	0.27	6078
VPH LR-R	28/10/2022	6158.3 – 7287.7	3×1200	0.31	6100

The measured flux densities for the PRS are shown, too. [†]Reimaged archival data from ref. 14. [‡] 3σ upper limits. ^{*}See the instrument cookbook. ^{*}Reciprocal linear dispersion. [†]Resolving power ($\lambda/\Delta\lambda_{\text{FWHM}}$).

Article

Extended Data Table 2 | FRB sample considered in this work

FRB Name	DM _{obs} ^a (pc cm ⁻³)	DM _{MW} ^b (pc cm ⁻³)	z ^c	d _L ^d (Gpc)	RM ^e (rad m ⁻²)	F _ν ^f (μJy)	ν ^g (GHz)	L _ν ^h (10 ²⁹ erg s ⁻¹ Hz ⁻¹)	References
FRB 20121102A	557	188	0.19273	0.98	1.4×10^5	180	1.7	2.1	1,2,3,4
FRB 20180916B	348.76	200	0.0337	0.15	-114.6	< 18	1.6	< 0.0048	5,6
FRB 20180924B	361.42	40.5	0.3214	1.74	14	< 20	6.5	< 0.72	7
FRB 20181112A	589.27	102	0.47550	2.76	10.9	< 21	6.5	< 1.91	8
FRB 20190520B	1204.7	113	0.241	1.25	-3.6×10^4	202	3	3.8	9,10
FRB 20200120E	87.8	55	0.0008	0.0036	-36.9	< 20	1.5	$< 3.1 \times 10^{-6}$	11,12
FRB 20201124A	413	140	0.0978	0.47	-889.5	20	15	0.053	13, this work
FRB 20210117A	729.1	34	0.214	1.10	43	< 10	6	< 0.15	14
FRB 20220912A	220	125	0.0771	0.36	-0.08	< 48	1.4	< 0.074	15,16
FRB 20110523A	623.3	43.52	$0.58^{+0.21}_{-0.21}$	$3.5^{+1.6}_{-1.4}$	-186.1	< 40	0.8	$< 5.8^{+6.6}_{-3.7}$	17
FRB 20150215A	1105.6	427.2	$0.69^{+0.22}_{-0.22}$	$4.3^{+1.7}_{-1.6}$	1.5	< 6.48	10.1	$< 1.4^{+1.4}_{-0.9}$	18
FRB 20150418A	776.2	188.5	$0.59^{+0.21}_{-0.21}$	$3.6^{+1.6}_{-1.4}$	36	< 70	1.4	$< 11^{+12}_{-7}$	19
FRB 20150807A	266.5	36.9	$0.17^{+0.10}_{-0.11}$	$0.85^{+0.57}_{-0.57}$	12	< 240	5.5	$< 2.1^{+3.7}_{-1.8}$	20
FRB 20160102A	2596.1	13	$3.04^{+0.51}_{-0.48}$	$26.4^{+5.4}_{-4.9}$	-220.6	< 30	5.9	$< 249^{+112}_{-84}$	21,22
FRB 20180309A	263.42	44.69	$0.16^{+0.10}_{-0.10}$	$0.79^{+0.57}_{-0.51}$	< 150	< 105	2.1	$< 0.8^{+1.5}_{-0.7}$	23
FRB 20191108A	588.1	52	$0.53^{+0.20}_{-0.20}$	$3.1^{+1.5}_{-1.3}$	474	< 213	1.4	$< 24^{+29}_{-16}$	24

RM measurements (or upper limits) and flux densities of the PRS are reported. ^aThe observed DMs of FRBs. ^bThe galactic DM contributions from the references or NE2001 from the FRB catalogue⁵⁷. ^cThe measured/inferred redshifts of FRBs. The redshifts in the top row are directly measured by the host galaxies of FRB. The redshifts in the bottom row are inferred by the extragalactic DMs; see ref. 9. The ΛCDM cosmological parameters are taken as $\Omega_m=0.315$, $\Omega_bh^2=0.02237$ and $H_0=67.36\text{ km s}^{-1}\text{ Mpc}^{-1}$ (ref. 58). ^dThe luminosity distance calculated by redshift. ^eThe observed RMs of FRBs. For the repeating sources, we take the largest absolute value for the observed RMs. ^fThe observed PRS flux densities. The upper limits here are corrected to the 3σ flux density limits. ^gThe measured frequencies of the PRS. ^hThe specific luminosities of the PRS inferred by the observed flux density and distance. References: (1)⁵⁹; (2)⁶⁰; (3)⁶¹; (4)²; (5)⁶²; (6)⁶³; (7)⁶⁴; (8)⁶⁵; (9)³; (10)⁶⁶; (11)⁶⁷; (12)⁶⁸ (13)⁴⁷; (14)⁶⁹; (15)⁷⁰; (16)⁷¹; (17)⁷²; (18)⁷³; (19)⁷⁴; (20)⁷⁵; (21)⁷⁶; (22)⁷⁷; (23)⁷⁸; (24)⁷⁹.

Extended Data Table 3 | Emission lines from the stacked spectra

Line	Param.	FRB reg.	Global
H α (1st comp.)	flux	3.03×10^{-15}	1.53×10^{-14}
	σ	2.97×10^{-17}	1.01×10^{-16}
H α (2nd comp.)	flux		1.01×10^{-14}
	σ		1.34×10^{-16}
H β	flux	1.19×10^{-15}	7.96×10^{-15}
	σ	7.68×10^{-17}	4.12×10^{-16}
[N II] 6584	flux	1.20×10^{-15}	9.69×10^{-15}
	σ	3.1×10^{-17}	1.67×10^{-16}
[O III] 5007	flux	5.63×10^{-16}	3.9×10^{-15}
	σ	5.03×10^{-16}	3.17×10^{-16}

Fluxes and uncertainties are in units of $\text{erg s}^{-1} \text{cm}^{-2}$. Fluxes are corrected for galactic extinction only.